# Image correction algorithm for functional three-dimensional diffuse optical tomography brain imaging

Yong Xu, Harry L. Graber, and Randall L. Barbour

We outline a computationally efficient image correction algorithm, which we have applied to diffuse optical tomography (DOT) image time series derived from a magnetic resonance imaging (MRI)-based brain model. Results show that the algorithm increases spatial resolution, decreases spatial bias, and only modestly reduces temporal accuracy for noise levels typically seen in experiment, and produces results comparable to image reconstructions that incorporate information from MRI priors. We demonstrate that this algorithm has robust performance in the presence of noise, background heterogeneity, irregular external and internal boundaries, and error in the initial guess. However, the algorithm introduces artifacts when the absorption and scattering coefficients of the reference medium are overestimated—a situation that is easily avoided in practice. The considered algorithm offers a practical approach to improving the quality of images from time-series DOT, even without the use of MRI priors. 

*OCIS codes:* 100.1830, 100.2980, 100.6890, 100.6950, 170.3010, 170.3880.

## 1. Introduction

As a technique for noninvasive monitoring of biomedical function, diffuse optical tomography (DOT) offers a number of practical, economic, and physiologic-informational advantages relative to other imaging modalities.[1,2] The technology is compact, can be brought to the bedside, and is easily combined with other imaging technologies. In addition, by extending the measurement to allow for the capture of a time series, it can explore various dynamic phenomena, in particular, those associated with the hemoglobin signal.

An important methodological complexity that analysis of these data brings is the need for computationally efficient reconstruction methods. Our approach to this has been to employ a first-order linear reconstruction algorithm[3,4] that, among other favorable attributes,[5] is computationally efficient. While we have shown that this method can recover dynamic features with good fidelity,[6–9] it would appear that the images produced have reduced spatial resolution and positional accuracy, when compared with results obtained using computationally intensive methods (i.e., iterative recursive image reconstruction algorithms).[10–13]

In a series of recent reports, we have developed an image correction methodology that significantly improves on these limitations in a manner that preserves computational efficiency.[14–18] The method applies a linear correction operator that is derived from knowledge of a position-dependent information spread function. The details of this function depend on both the algorithm and the measurement geometry, but it is easily computed for any specific case. Insight into this approach was derived from an understanding of principles used in magnetic resonance imaging (MRI). In particular, we extended the idea of frequency encoding of spatial information to an analogous temporal encoding scheme that serves to identify how spatial information from the object domain is mapped to the image domain.

While previous reports have demonstrated that the linear correction method is effective, these results were based on test media that were idealized in several respects.[15–18] They were regular shapes with smooth external boundaries, convex everywhere, and had structural heterogeneity that consisted of a small

The authors are with the Department of Pathology, SUNY Downstate Medical Center, Box 25, 450 Clarkson Avenue, Brooklyn, New York 11203. R. L. Barbour's e-mail address is rbarbour@downstate.edu.

Received 10 July 2006; revised 7 November 2006; accepted 8 November 2006; posted 8 November 2006 (Doc. ID 72863); published 13 March 2007.

0003-6935/07/101693-12$15.00/0

number of spherical inclusions embedded in homogeneous, static backgrounds. Also, they were limited to media having perturbations in only the absorption coefficient. For this paper, we have expanded our examination to systematically explore the effect of target medium complexity on the performance of the correction scheme, based on computational models of the head derived from 3D magnetic resonance images.

## 2. Methods

### A. Target Medium Structure

The starting point for the geometric model used here was a 3D T1-weighted structural MRI of the human head [GE Medical Systems SIGNA, 1.5T, TR = 35 ms, TE = 5 ms, tip angle = 45°, 3D GRASS (Gradient Recalled Acquisition in Steady State) pulse sequence], publicly available in the form of 60 3 mm thick coronal-section DICOM (Digital Imaging and Communications in Medicine) images.[19] The particular section shown in Fig. 1, which lies at the level of the temporal bone to the midmandible and has a maximal horizontal total width of ~12.5 cm, intersects the premotor and primary motor cortices. The region indicated by a dashed outline (~6 cm along the surface, 3 cm in depth) in Fig. 1, whose dimensions are typical of the tissue volume interrogated in our dynamic DOT brain-imaging studies,[20] was chosen as the basis of a heterogeneous target medium for use in simulation studies. Six principal tissue types—scalp, muscle, skull, cerebrospinal fluid (CSF), gray matter, and white matter—were identified within the selected area, and the interfaces between them, as well as the exterior boundary, were traced. A 2D finite-element model was created, with a commercial mesh-generating package,[21] taking the selected region's borders and inter-tissue-type interfaces as the boundaries of subregions, each of which is denoted by a different gray level in Fig. 2(a). Next, a model with 3D geometry was generated by extruding the 2D model in the orthogonal ($z$, by definition) direction, thereby producing the cylinder (i.e., the geometry is 3D, but heterogeneous in only the $x$ and $y$ dimensions) depicted in Fig. 2(b). Finally, an additional small subvolume was created within the gray matter region of the 3D model, having no boundary in common with the model's external surfaces, as shown in Fig. 2(c). This volume can be interpreted either as the portion of cerebral cortex that is activated by a specific task or as a tumor or other lesion.

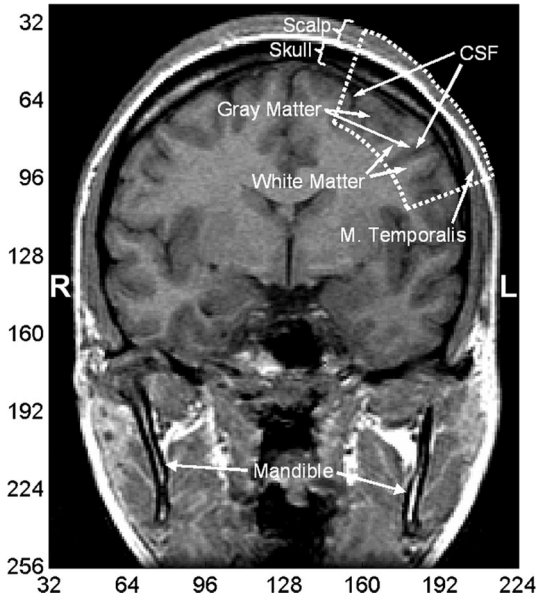

Fig. 1. Tissue model used to generate simulated data. The section shown intersects the premotor and primary motor cortices.

### B. Target Medium Optical Properties

#### 1. Static Heterogeneity

Among the different physiological compartments in the model, CSF has substantially weaker absorption and scattering than surrounding tissues. In contrast, differences between optical coefficients of the other tissue types is of the same order of magnitude as the variability within the values reported for each type.[22,23] Accordingly, heterogeneous media were modeled by assigning one pair of absorption-coefficient ($\mu_a$) and scattering-coefficient ($\mu_s$) values to the inclusion, a second pair to the CSF, and a third to all other compartments. Also, since an activated region, as well as certain types of lesions, would be expected to absorb near-infrared (NIR) light more strongly than the surrounding unaffected tissue, a higher $\mu_a$ was assigned to the inclusion than to the other tissue types. The optical coefficients used were: $\mu_s = 10$ cm$^{-1}$, $\mu_a = 0.24$ cm$^{-1}$ in the inclusion; $\mu_s = 10, 5, 1$, or $0.5$ cm$^{-1}$, $\mu_a = 0.08, 0.04, 0.01$, or $0.005$ cm$^{-1}$ in the CSF compartment; $\mu_s = 10$ cm$^{-1}$, $\mu_a = 0.08$ cm$^{-1}$ elsewhere. The specific permutations of $\mu_a$ and $\mu_s$ values modeled are given in Table 1.

#### 2. Optical Coefficient Dynamics

Sinusoidal temporal variation was imposed on the absorption coefficient in two of the model tissue compartments, in order to explore spatial blurring of dynamic information and our ability to spatially isolate it.

The time-varying absorption assigned to the gray matter and inclusion volumes were

$$\mu_{ag}(t) = \mu_{ag0}[1 + m_r \sin(2\pi f_r t + \varphi_r) + m_c \sin(2\pi f_c t + \varphi_c)] \quad (1)$$

for the gray matter (hence the subscript $g$), and

$$\mu_{ai}(t) = \mu_{ai0}[1 + m_v \sin(2\pi f_v t + \varphi_v)] \quad (2)$$

for the inclusion (subscript $i$). Plots of Eqs. (1) and (2) are shown in Fig. 3. The mean-absorption coefficient values $\mu_{ag0}$ and $\mu_{ai0}$ were taken from Table 1, while the modulation frequencies were $f_r = 0.1$ Hz ($r$ = respiratory), $f_c = 1.0$ Hz ($c$ = cardiac) and $f_v = 0.06$ Hz ($v$ = vasomotor). The corresponding initial phases were $\varphi_c = \varphi_r = \varphi_v = \pi/2$, and the modulation depths were $m_c = 0.02$, $m_r = 0.1$, $m_v = 0.2$.

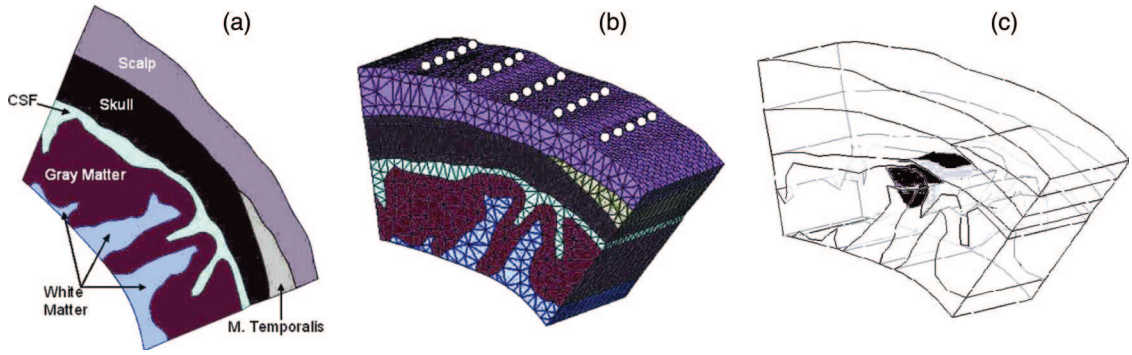


Fig. 2. (Color online) (a) Two-dimensional heterogeneous model geometry, with the subregions coded by gray levels, derived from the portion of Fig. 1 bounded by a dashed curve. (b) Exterior view of the 3D model geometry generated by extruding the 2D model in the third dimension, with source and detector positions indicated as small white circles. (c) Interior view of the 3D model from Fig. 2(b), revealing the inclusion embedded in gray matter.

The forward- and inverse-problem computations described below were carried out for a total of 100 successive time frames, with a time interval $\Delta t = 0.5$ s.

### C. Forward Problem

Shown in Fig. 2(b) are the 25 simulated source and detector locations for the simulated DOT measurements reported on here. Taking the curvature of the surface into account, the maximum source-detector separation is ~5 cm (~1 cm spacing between rows and ~0.67 cm between adjacent positions within a row). The array depicted closely approximates the arrangement of optical fibers typically used in performing neurological function (e.g., finger-tapping) studies,[20,24] or other measurements of hemodynamics associated with specific activation of the premotor and/or primary motor cortices.

All surface detector data and internal photon intensities were obtained by performing finite-element method (FEM) computations to numerically solve the diffusion equation with Robin boundary conditions.[3,4] Each forward-problem computation was performed four times, once for each set of optical coefficients assigned to the CSF (Subsection 2.A and Table 1).

Three distinct FEM meshes were generated from the multiple-compartment model geometry described in Subsection 2.A, differing in their numbers of mesh nodes. The coarsest (1339 nodes) is used for inverse-problem computations (image reconstruction, spatial correction), as described below. The intermediate-density mesh (4375 nodes) is used for computation of the detector data that enter into the generation of image correction matrices (Subsection 2.E),[15–17] and the reference-medium detector readings and interior photon intensities that enter into the image-reconstruction calculations (Subsection 2.D). The finest mesh [5360 nodes, and the one depicted in Fig. 2(b)] is used for computation of detector data, for the media containing an inclusion with properties distinct from those of the surrounding tissues (Table 1: Target1–Target4).

When the dynamic (100 time frames) algorithm-testing data were computed, the inclusion was assigned a time-averaged $\mu_a$ different from those of the other compartments, as described above. However, when the time-series ($2^{14}$ time frames) simulations needed for computation of image correction matrices were carried out, the inclusion region was assigned the same time-averaged $\mu_a$ as the other non-CSF compartments (Table 1: Reference1–Reference4). Static media (i.e., one time frame) were used for the reference-medium detector reading and interior-intensity computations, with the $\mu_a$ of the inclusion

**Table 1. Optical Coefficient Values Assigned to the Different Tissue Compartments, for All Target and Reference Media[a]**

| | CSF | | Inclusion | | Others | |
|---|---|---|---|---|---|---|
| Calculation | $\mu_s$ ($cm^{-1}$) | $\mu_a$ ($cm^{-1}$) | $\mu_s$ ($cm^{-1}$) | $\mu_a$ ($cm^{-1}$) | $\mu_s$ ($cm^{-1}$) | $\mu_a$ ($cm^{-1}$) |
| Target1 | 10.0 | 0.080 | 10.0 | 0.24 | 10.0 | 0.08 |
| Target2 | 5.0 | 0.040 | 10.0 | 0.24 | 10.0 | 0.08 |
| Target3 | 1.0 | 0.010 | 10.0 | 0.24 | 10.0 | 0.08 |
| Target4 | 0.5 | 0.005 | 10.0 | 0.24 | 10.0 | 0.08 |
| Reference1 | 10.0 | 0.080 | 10.0 | 0.08 | 10.0 | 0.08 |
| Reference2 | 5.0 | 0.040 | 10.0 | 0.08 | 10.0 | 0.08 |
| Reference3 | 1.0 | 0.010 | 10.0 | 0.08 | 10.0 | 0.08 |
| Reference4 | 0.5 | 0.005 | 10.0 | 0.08 | 10.0 | 0.08 |

[a]For tissue types with dynamic $\mu_a$, tabulated number is the temporal mean assigned to the different tissue compartments, for all target (Target1–Target4) and reference: (Reference1–Reference4) media.

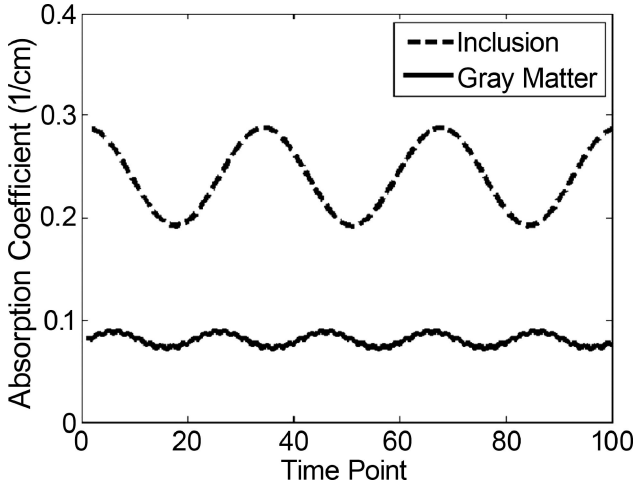


Fig. 3. Plots of $\mu_a$ versus time, in the inclusion and gray-matter compartments of the 3D tissue model of Figs. 2(b) and 2(c).

and gray-matter compartments set equal to the gray-matter temporal mean value, $\mu_{ag0}$.

### D. Inverse Problem

Images were reconstructed by using the previously described normalized difference method (NDM),[3] which is a modified linear perturbation technique that is highly robust to many difficult-to-eliminate sources of experimental error and uncertainty associated with DOT measurements. In the NDM, the fundamental relation between detector data and medium optical properties, for a given measurement wavelength used for DOT measurements, is

$$\left(\frac{R-R^0}{R^0}\right)_j R_j^r = \sum_k \left(w_{jk}^a \Delta\mu_{a,k} + w_{jk}^s \Delta\mu_{s,k}\right), \qquad (3)$$

where $j$ and $k$ index the source-detector channels and FEM mesh nodes, respectively. $R_j$ is the $j$th-channel detector data for a particular time frame, and $R_j^0$ is the $j$th-channel baseline value; $R_j^r$ is the $j$th-channel detector data acquired from a reference medium whose optical coefficients are thought to closely approximate those of the target medium; $w_{jk}^a$ and $w_{jk}^s$ are elements of the transformation, or weight, matrix that relates optical coefficient perturbations within the reference medium to their effects on data recorded at its surface; $\Delta\mu_{a,k}$ is the difference, at the $k$th FEM mesh node, between the absorption coefficients of the target and reference media; and $\Delta\mu_{s,k}$ is the analogous perturbation of the scattering coefficient. Forward-problem computations performed on the intermediate-density FEM mesh (see Subsection 2.C) are used in the computation of $R_j^r$, $w_{jk}^a$, and $w_{jk}^s$. The latter two quantities are functions of photon intensities, and of their spatial gradients, within the reference medium.[25,26] To minimize the computational effort for the inverse problem, solutions were based on a coarse mesh (1339 nodes). To retain accuracy for the forward problem, results were initially computed using the intermediate mesh density and then interpolated to the course mesh.[27] Inverse solutions were obtained using regularized LU decomposition.[18] Mirroring the forward-problem computations, the number of time frames was 100 for the Target1–Target4 time series, and $2^{14}$ for the Reference1–Reference4 time series. The latter calculation took less than 10 min to perform on a 2.8 GHz PC with 1 Gbyte of RAM.

To examine the effect of random error on the accuracy of recovered images, reconstructions and image corrections were conducted four times. Noise-free detector data were used in the first instance, and Gaussian white noise was added to the normalized detector data in the remaining three. [The normalized detector reading for detector channel $j$ is $(R/R^0)_j$.] As in previous reports, here we used a noise model in which the noise level (i.e., the standard deviation of the noise distribution) is a preselected percentage—which grows as the fourth power of the distance between source and detector— of the noise-free detector reading.[18] In the noise-added trials, the minimal noise level (source and detector colocated) was 1%, 2% or 3%, while the maximal noise level was, respectively, 10%, 20%, or 30%. The noise distributions used for each trial were stationary, i.e., the noise levels were not time varying.

The impact of systematic error in the estimates of time-averaged tissue optical coefficients was studied by pairing detector data computed for one assignment of CSF $\mu_a$ and $\mu_s$ with a weight matrix computed for a different set of CSF properties. All 16 target–reference combinations have been examined.

### E. Image Correction

Images reconstructed by solving Eq. (3) were post-processed via the image-correction algorithm that we have previously described,[15–18] which is based on a numerical direct assessment of the information-distorting properties of inverse-problem algorithms. We proceed by first generating a time series of medium states $\mathbf{M}$ (a $N_n \times N_t$ matrix, where here the number of FEM mesh nodes is $N_n = 1339$, and the number of time frames is $N_t = 2^{14}$), with distinguishable functional forms assigned to the $\mu_a$ dynamics of the nodes, and then computing the corresponding time series of reconstructed images $\hat{\mathbf{M}}$. Then the image correction matrix, or filter, is simply the least-squares solution of the overdetermined linear system $\mathbf{M} = \mathbf{F}\hat{\mathbf{M}}$. Here, $\mathbf{F}$ is a square, $N_n \times N_n$ matrix whose $k$th row is an estimator for the true optical-coefficient perturbation at the $k$th node. To control for ill conditioning, calculations of solutions to $\mathbf{M} = \mathbf{F}\hat{\mathbf{M}}$ (which took less than 10 min on the same PC as used for reconstructing images) employed the same zeroth-order Tikhonov regularization method as was used in solving Eq. (3).

After an image-correction matrix $\mathbf{F}$ has been generated, any image $\hat{\mathbf{m}}$ that is subsequently reconstructed by using the same mesh and source-detector geometry, and the same reconstruction algorithm as was used for

the computation of $\hat{\mathbf{M}}$, can be spatially corrected via a simple matrix multiplication: $\mathbf{m} = \mathbf{F}\hat{\mathbf{m}}$.

Four image-correction matrices $\mathbf{F}_1$–$\mathbf{F}_4$ were generated, corresponding to the four spatial distributions, Reference1–Reference4, of $\mu_a$ that are considered here (see Table 1). In the systematic-error study, each image-reconstruction weight function is paired with the corresponding image-correction matrix, computed for the same assumed values of CSF $\mu_a$ and $\mu_s$. Thus we are able to determine the sensitivity of this image-enhancement strategy to uncertainty–imprecision in our knowledge of background optical coefficients. Computations of $\mathbf{F}_1$–$\mathbf{F}_4$ employed the same interpolation from the intermediate density to coarse mesh, as described in Subsection 2.D, for both the assigned reference-medium coefficient values and weight matrices.

### F. Noise Suppression

The spatially corrected images that were recovered from noisy detector data were subsequently treated with three noise-suppression schemes. The first method was temporal low-pass filtering (tLPF) with a zero-phase finite impulse response digital filter, using a trapezoidal frequency-response function with threshold frequency set to 0.15 Hz and a 0.05 Hz roll-off (i.e., all frequencies lower than 0.125 Hz are fully passed, all frequencies greater than 0.175 Hz are completely blocked, and the frequency response decreases linearly over the 0.125–0.175 Hz interval). The second noise-suppression scheme was "pillbox" spatial low-pass filtering (sLPF), wherein the image value at each FEM node is replaced by a weighted average of the values at that node and its near neighbors.[28] The third approach employed both the tLPF and sLPF operations. The effects of these procedures were quantified by computing the spatial and temporal correlations of the recovered images before and after each one (see Subsection 2.6).

The tLPF operation was applied to the data time series in each image pixel individually, without regard to information present in other pixels. It should also be noted that absolute frequencies are enumerated in the preceding paragraph, i.e., they are not normalized to the Nyquist frequency. But as the latter was precisely 1 Hz (see Subsection 2.B.2), here the normalized and unnormalized frequencies are equal.

### G. Quantification of Image Accuracy

The spatial and temporal correlations between target medium and reconstructed images are used here as the indices of spatial and temporal accuracy, respectively, of recovered images.[18] The spatial correlation (SC) at a given time frame $t_0$ is defined as

$$\mathrm{SC}(t_0) = \frac{1}{N_n - 1} \sum_{k=1}^{N_n} \left( \frac{u_k - \bar{u}}{s_u} \right) \left( \frac{v_k - \bar{v}}{s_v} \right), \tag{4}$$

where $u_k = u(\mathbf{r}_k, t_0)$ is the true value of the $\mu_a$ perturbation at the $k$th FEM mesh node of the target medium, $v_k = v(\mathbf{r}_k, t_0)$ is the corresponding $\mu_a$ perturbation of the recovered image, $\bar{u}$ and $\bar{v}$ are the spatial mean values of $u$ and $v$, $s_u$ and $s_v$ are the corresponding spatial standard deviations, and the summation runs over all $N_d$ mesh nodes (here, $N_n = 1339$). The temporal correlation (TC) at a given location $\mathbf{r}_0$ is defined as

$$\mathrm{TC}(\mathbf{r}_0) = \frac{1}{N_t - 1} \sum_{k=1}^{N_t} \left( \frac{u_k - \bar{u}}{s_u} \right) \left( \frac{v_k - \bar{v}}{s_v} \right), \tag{5}$$

where $u_k = u(\mathbf{r}_0, t_i)$ and $v_i = v(\mathbf{r}_0, t_i)$ are contrast parameter values of the target medium and reconstructed image, respectively, and the summation runs over all $N_t$ time points (here, $N_t = 100$). In Eq. (5), $\bar{u}$ and $\bar{v}$ are temporal mean values, and $s_u$ and $s_v$ are temporal standard deviations. All subsequently reported TC values are spatial averages over the inclusion volume only. While this restriction was made principally for convenience, our examination of the region of interest does not degrade our ability to explore the spatial convolution of gray matter and inclusion volume, as this effect will be manifested by a reduced value of the computed TC.

For the purpose of quantifying the degree of improvement or degradation of image quality that is associated with spatial image correction, relative differences between the SC and TC after versus before this procedure frequently is more informative than the raw indices computed using Eqs. (4) and (5). Accordingly, the relative percent changes (RPCs) in SC and TC also have been computed, via the formulas

$$\mathrm{RPC}_s = 100 \frac{\mathrm{SC}_c - \mathrm{SC}_u}{\mathrm{SC}_u}, \tag{6}$$

$$\mathrm{RPC}_t = 100 \frac{\mathrm{TC}_c - \mathrm{TC}_u}{\mathrm{TC}_u}, \tag{7}$$

where the subscripts $u$ and $c$ indicate the correlations computed for the images prior to and subsequent to image correction.

## 3. Results

### A. Influence of Reference-Medium Mismatch

#### 1. *Noise-free Data*

In practice, it can be expected that application of the image-correction scheme will involve a mismatch between the actual background properties of the target medium and those assumed for the purpose of computing the image formation ($\mathbf{W}$) and correction ($\mathbf{F}$) operators. Here we explore the influence this systematic error has on our ability to improve image quality. To do this, we have computed the effects that application of the correction scheme has on the set of all target–reference combinations (16 pairings). These combinations explore the influence of over- and underestimation of the background optical properties, in particular those associated with the CSF. We consider this because CSF is the one compartment most

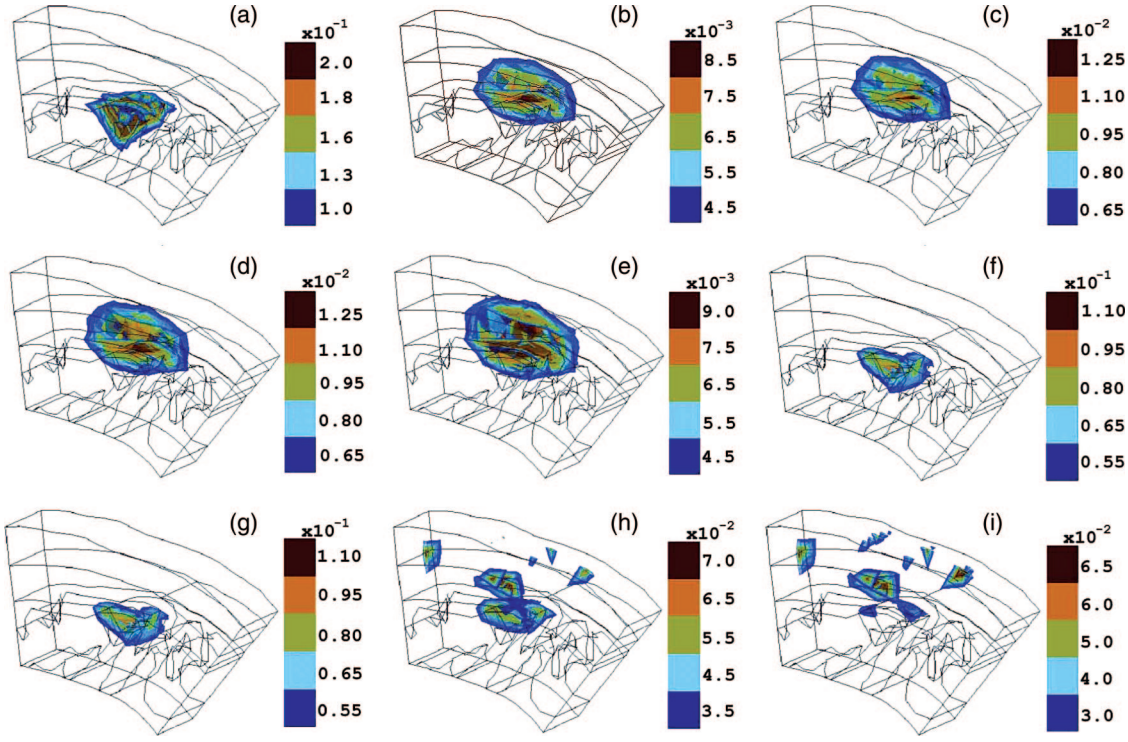


Fig. 4. (a) Volume rendering of the Target2 target medium, at time frame 100. (b)–(e) Volume renderings of images reconstructed from Target1–Target4 detector data, respectively, by solving Eq. (3). For all four targets, the $R^r$, $w^a$, and $w^s$ factors are computed from the Reference2 medium (see Table 1). (f)–(i) Volume renderings of the Target1–Target4 images, respectively, after they have been spatially deconvolved, using the method of Subsection 2.E. In each subfigure, the range of $\mu_a$ values plotted runs from $\mu_a^{\max}/2$ to $\mu_a^{\max}$.

likely to have variations in its optical properties in cases of pathology [e.g., subdural hematoma, cerebral sepsis, liver disease (i.e., jaundice)].

Shown in Fig. 4 are results documenting the image improvement achieved using the type-2 reference, applied to each of the four targets. Note that, because of the relative independence of image quality on the temporal variations in inclusion and background properties, here we show only one of the 100 images in each target image time series. Inspection shows that prior to image correction, the location of the recovered inclusion is closer to the surface than its true position, its maximum amplitude is <6% of its true value, and its size is overestimated. In addition, this trend is mainly independent of the mismatch between the true and assumed background medium properties, which is a finding consistent with properties of the NDM algorithm.[3] Application of the correction procedure produces images that have much greater location and coefficient accuracy (at least for Target1 and Target2) but tend to underestimate the inclusion size. It is worth emphasizing that the latter is mainly a consequence of the minimum threshold value, which by convention was 50% of the maximum image value. Careful inspection of the coefficient gradient in the recovered image shows that this function is much steeper in the corrected image than in the uncorrected one and is a finding we have consistently seen in many other test cases.[16–18] Reinforcing this consideration are results shown in Fig. 5, which documents a large improvement in the spatial correlation following image correction. The other finding of interest indicated in Fig. 4 is that use of a correction matrix corresponding to an overestimate of the background optical coefficients quickly leads to a degradation in the quality of the corrected image. As detailed in Fig. 5, this trend seems to hold for other target–reference pairs as well, but the reverse bias (i.e., using a correction operator that underestimates the background optical coefficients) is much more robust to such systematic errors.

Shown in Fig. 5 are the relative changes in the spatial and temporal correlations as a consequence of applying the image-correction scheme, for the complete set of target–reference combinations. It is not surprising that the optimal improvement was seen when the background properties of the reference match those of the target. In the case of spatial correlation, this improvement was in the range of 50%–62% depending on the particular target considered (maximum SC value obtained was 0.61). Qualitatively similar findings were seen for TC, but here the improvement was more modest. This quantitative difference, however, is not owing to any inherent limitation in the ability to accurately recover temporal behavior. Rather, it is because the value obtained was already nearly optimal (0.94–0.95 for uncorrected images, 0.96–0.99 for corrected images).

Also shown in Fig. 5 is the influence of a mismatch between the backgrounds of the target and reference.

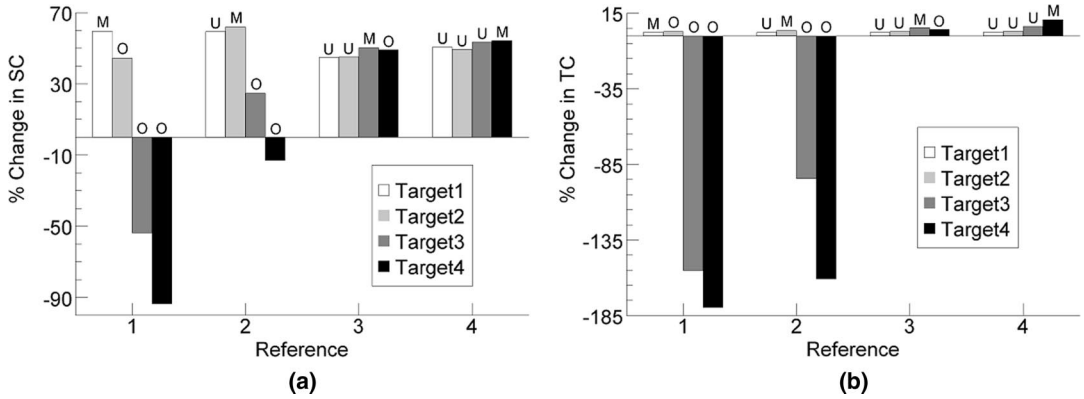


Fig. 5. (a) Bar graph of relative percent change in image spatial correlation, comparing the image-to-target SC [Eq. (4)] after and before spatial image correction, for all 16 target–reference pairings. (b) Bar graph of the corresponding RPCs in image TC. Each bar represents the average $RPC_s$ [Eq. (6)] or $RPC_t$ [Eq. (7)] across all 100 time frames. Annotations indicate whether the reference-medium CSF optical coefficients match (M), overestimate (O) or underestimate (U) those of the target medium.

Inspection shows that when the reference background optical coefficients overestimate those of the target, the SC and TC quickly decline. In contrast, when the bias is reversed, the accuracy measures are stable and indicate that the corrected images have significantly improved spatial accuracy and retain good temporal accuracy. It is also worth noting that the SC findings obtained were mainly independent of fluctuations in background mismatch caused by the temporal variability in the inclusion and gray matter (results not shown).

### 2. *Impact of Noise*

The influence of measurement data noise on image correction is shown in the results presented in Figs. 6–8. Seen in Fig. 6 are results obtained when the background properties for the target and reference are matched. Each column corresponds to a different noise level: 1%–10% in Figs. 6(a), 6(d), and 6(g), 2%–20% in Figs. 6(b), 6(e), and 6(h), and 3%–30% in Figs. 6(c), 6(f), and 6(i). Each row corresponds to a different treatment of the imaging data: in Figs. 6(a)–6(c), images have been reconstructed and corrected, but no

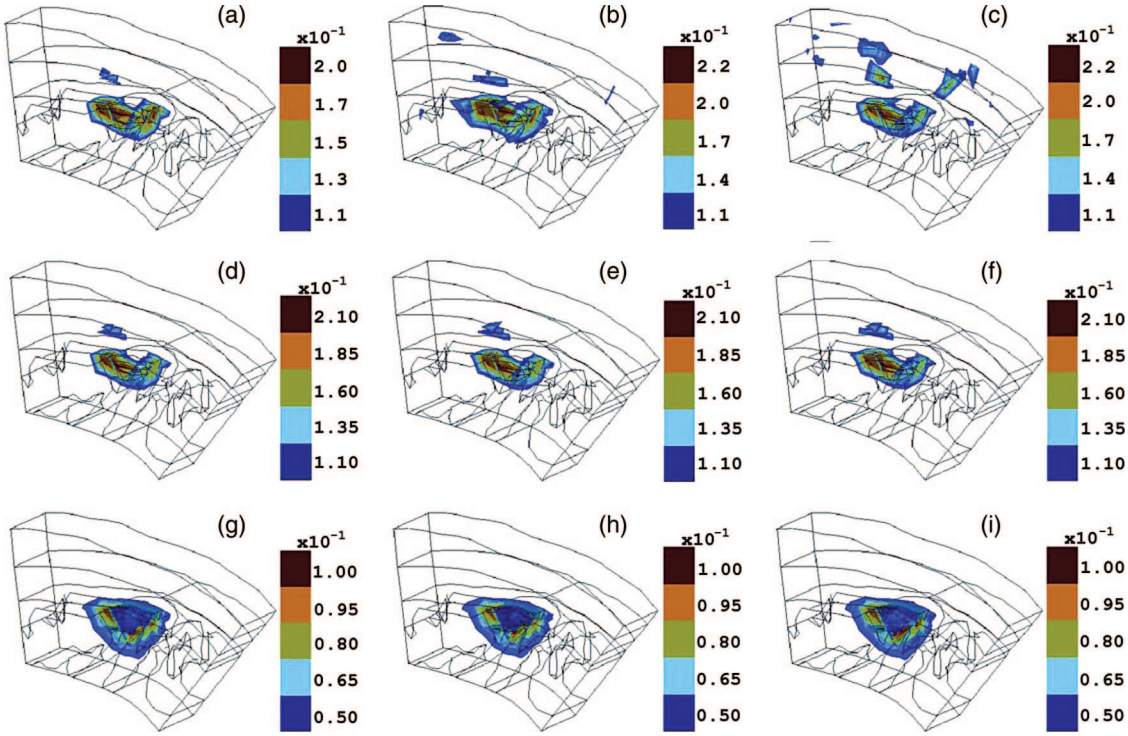


Fig. 6. Spatially corrected images, for time frame 100, reconstructed from noisy detector data. (a), (d), (g) Noise level 1: noise standard deviation is 1%–10% of noise-free detector reading. (b), (e), (h) Noise level 2: noise standard deviation is 2%–20% of noise-free detector reading. (c), (f), (i) Noise level 3: noise standard deviation is 3%–30% of noise-free detector reading. (a)–(c) No noise suppression method is used. (d)–(f) tLPF used to suppress noise. (g)–(i) sLPFs and tLPFs used to suppress noise.

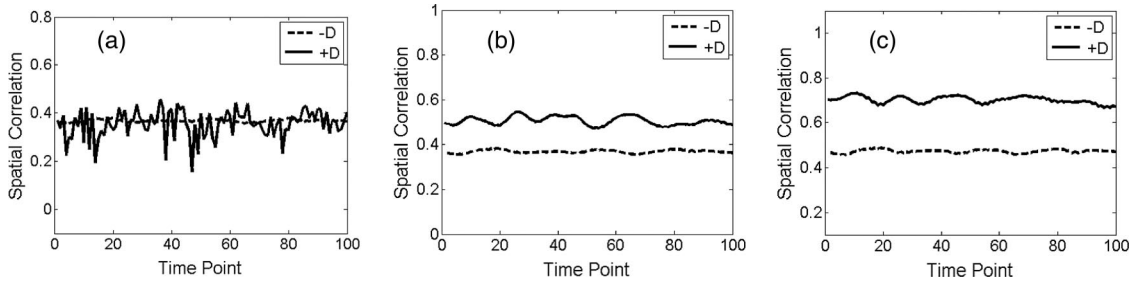


Fig. 7. Plots of image-versus-target spatial correlation versus time frame, before (dashed curves) and after (solid curves) spatial correction, for images recovered from data contaminated with level-3 noise. (a) No noise-suppression method is used. (b) tLPF used to suppress noise. (c) sLPFs and tLPFs used to suppress noise. −D = uncorrected image, +D = corrected image.

noise suppression technique has been applied; in Figs. 6(d)–6(f), a tLPF has been applied to the image time series after the correction step; and in Figs. 6(g)–6(i), a sLPF has been applied to the corrected and temporally filtered images. The primary manifestation of noise is the appearance of superficial artifacts in the image, whose magnitude and number increase with noise level [similar to the ones seen in Figs. 4(h) and 4(i)]. Unlike the systematic-error results, however, these are not associated with appreciable losses in quantitative accuracy. Application of the tLPF reduces but does not eliminate the artifacts, and does not have any noticeable impact on the size, shape, location, or on quantitative accuracy of the recovered inclusion. The images that are denoised with both temporal and spatial LPFs, and the analogous sLPF-only denoised images (not shown), retain none of the artifacts. In addition, the recovered inclusion more closely approximates the ideal shape [see Fig. 4(a)] after application of the sLPF than before. These improvements, however, come at the cost of lower quantitative accuracy.

The time dependence of the image SC computed from noisy data and the ameliorating effects of the denoising operations are illustrated in Fig. 7. Results presented here are derived from data with the highest, 3%–30%, noise level considered. Prior to the application of any denoising technique [Fig. 7(a)], the uncorrected-image SC, while low, is nearly constant across time. Furthermore, its average value of 0.37 is less than 0.5% lower than the average SC for noise-free data. The SC for the corrected images is more variable across time, with a mean value of 0.35. The latter number is significantly worse than the 0.55 average SC that is computed from noise-free data (corresponding averages for the 1%–10% and 2%–20% noise level are 0.51 and 0.43, respectively). Following application of the tLPF [Fig. 7(b)], the uncorrected-image SC is nearly indistinguishable, in both average value and temporal variability, from the noise-free-data SC (not shown). The same noise-suppression scheme yields a 0.51 average SC, which is only 1.2% lower than the corresponding noise-free value, for the corrected-image time series, but with significantly greater temporal variability than in the noise-free results. Marked improvements in the SCs of both uncorrected and corrected images are produced by using both the tLPF and the sLPF [Fig. 7(c)]. The average uncorrected-image SC is 0.47, and the average corrected-image SC is 0.7, when temporal and spatial filtering are used in tandem. The former value is only 0.5% greater than the average uncorrected-image SC obtained when only the sLPF technique is used to suppress noise, but the latter is significantly higher than the 0.53 average sLPF-only SC of the corrected images. Thus these results demonstrate that the combination of temporal and spatial LPFs produces the highest quality corrected image, and that the dual-LPF result is appreciably better than that produced by either one alone.

In agreement with a previous report,[18] we find that in the presence of noise, image correction typically is associated with a lower TC in the inclusion region, but that using LPFs can minimize the reduction. Examination of TCs computed for different target–reference pairings and noise levels gives results that largely parallel those for spatial accuracy: the best final result (i.e., TC closest to that of the original, uncorrected image) is obtained when both temporal and spatial LPFs are used. An important difference in detail is that, when the noise-suppression methods are ranked in order of the degree of improvement obtained, we get sLPF + tLPF > tLPF > sLPF for the TC and sLPF + tLPF > sLPF > tLPF for the SC. Additionally, when the highest noise level is combined with a reference that overestimates the CSF optical coefficients of the target (i.e., the worst case in terms of both systematic and random errors), image correction tends to cause a reversal of the algebraic sign of the TC. This is not remedied by the application of either or both types of LPF.

Summarizing the preceding descriptions, Fig. 8 shows contour maps of ($RPC_s$ [Fig. 8(a)] and $RPC_t$ [Fig. 8(b)], for all four Target$N$–Reference3 pairings and all three noise levels. As in the systematic-error study, positive (negative) values indicate that the correlation is higher (lower) after image correction than before. Inspection of these plots shows that at the lowest noise level, which is typical of data collected in DOT brain measurements, the SC invariably increases upon image correction. We also see that irrespective of the noise level, the percentage increase in SC can be made larger by using LPFs, especially

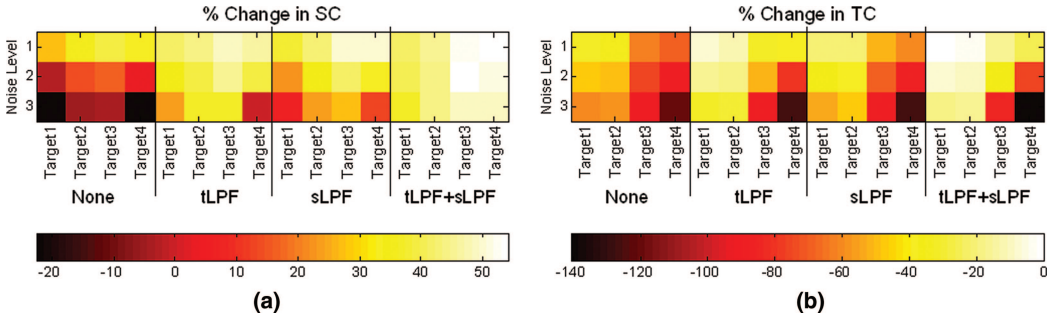


Fig. 8. (Color online) (a) Contour map of RPC in image spatial correlation, comparing the image-versus-target SC [Eq. (4)] after and before spatial correction, for the four Target*N*–Reference3 pairings, three noise levels, and four varieties of noise suppression. (b) Contour map of the corresponding RPCs in image temporal correlation. Each square represents the average $RPC_s$ [Eq. (6)] or $RPC_t$ [Eq. (7)] across all 100 time frames.

sLPF and tLPF in combination. At the lowest noise level, the loss of TC associated with image correction can also be minimized by using sLPF and tLPF in combination. Furthermore, at *all* noise levels, the loss of TC can be kept within acceptable limits, provided that the reference-medium CSF optical coefficients do not overestimate those of the target medium.

### B. Image Correction without Anatomical Prior Information

A secondary issue we have considered is that, even though the use of anatomical priors can be advantageous, in practice this involves an added effort for which automated routines are generally not available. It is thus useful to explore whether effective alternative strategies can be found. One possible approach is to employ nonlinear reconstruction methods to yield a heterogeneous reference medium, from which the image-reconstruction and image-correction operators are computed. It should be noted that the computational burden for this approach is a small fraction of that for most iterative reconstruction methods, in that the updating process need be carried out only once, and is not repeated for each time frame.

Results in Table 2 identify the image quality improvements that can be achieved, for the four targets considered here, when the above approach was implemented. For comparison, the corresponding values for homogeneous-reference and MRI-based-reference image reconstructions also are included. All values in the table were computed from noise-free images. The highlighted entries are those for which there is a match between the optical parameters of the target and reference media. An intuitive expectation is that these would have the highest SC and TC among the three approaches, and that in all cases the iterative-update result would be intermediate between the other two. With the exception of the uncorrected-image SC, where the iterative approach produced values higher than those for the MRI priors, this expectation is observed.

In detail, it is seen that SC for uncorrected images is higher under the iterative-update approach than for either of the others but remains low overall. The SC for the corrected-image results is never maximal for the iterative-update data, and this approach does not yield as much relative improvement as the MRI-prior method (average $RPC_s = 27\%$ for the former and 47% for the latter). Moreover, the iterative-update approach always gives qualitatively improved corrected images, even though its starting point is the same homogeneous reference medium that degrades image quality in the mismatched cases (Target3–Reference1 and Target4–Reference1 pairings).

With regard to recovery of dynamic information, it is seen that the uncorrected-image TC value is dependent on the strategy for computing the reference medium. The ordering observed is MRI prior > iterative update > homogeneous reference for all four targets. The MRI-prior > iterative-update ordering holds for the corrected-image TC results as well.

**Table 2. Spatial and Temporal Image-Versus-Target Correlations, before and after Image Correction, for Different Strategies for Applying the Correction Scheme[a]**

| | SC | | | | | | TC | | | | | |
|---|---|---|---|---|---|---|---|---|---|---|---|---|
| | Uncorrected | | | Corrected | | | Uncorrected | | | Corrected | | |
| Target Medium | Homogeneous | Iterative | Prior | Homogeneous | Iterative | Prior | Homogeneous | Iterative | Prior | Homogeneous | Iterative | Prior |
| Target1 | **0.339** | 0.371 | 0.353 | **0.541** | 0.462 | 0.511 | **0.938** | 0.948 | 0.958 | **0.961** | 0.925 | 0.980 |
| Target2 | 0.345 | 0.379 | 0.363 | 0.498 | 0.485 | 0.527 | 0.939 | 0.947 | 0.958 | 0.966 | 0.931 | 0.986 |
| Target3 | 0.333 | 0.382 | **0.368** | 0.154 | 0.499 | **0.554** | 0.909 | 0.917 | **0.934** | −0.503 | 0.920 | **0.984** |
| Target4 | 0.324 | 0.381 | 0.368 | 0.0206 | 0.480 | 0.549 | 0.849 | 0.870 | 0.891 | −0.677 | 0.571 | 0.928 |

[a]Highlighted entries indicate exact match between the optical coefficients of the target and the reference media.

However, when the homogeneous-reference and iterative-update approaches are compared, the ordering is medium dependent. The homogeneous reference yields the higher corrected-image TC for Target1 and Target2, while for Target3 and Target4 the iterative-update approach performs significantly better. Overall, we find that even a single update of the reference-medium estimate allows for generation of corrected images that are substantially similar to those obtained using the MRI priors.

#### 4. Discussion

Time-series DOT, with its capacity to explore the temporal dynamics of the hemoglobin signal using compact and portable technology, provides new opportunities to explore the spectrum of functional states associated with blood delivery to tissue. Given the expectation that a single study can generate data corresponding to thousands to tens of thousands of volumetric images, consideration of the computational effort required to analyze this data is key to developing practical systems. First proposed by our group was a linear perturbation formulation,[29,30] which has since been adopted by many other groups.[31–34] In principle, this strategy can yield absolute measures of tissue chromophore levels. In practice, however, experimental uncertainties, such as imperfect knowledge of external tissue geometry, tissue optical properties, transmission efficiencies of the measuring system, and contact fidelity between optodes and tissue, produce solutions that are easily biased. Recognizing that measures of relative changes in biological signal levels are often useful, we later introduced a modified formulation based on such variations that has proven robust to many of the experimental uncertainties.[3] Characterization of this method has shown that dynamic phenomena can be recovered with remarkable accuracy, even in the limit of spatiotemporal coincident states.[5] As the method is limited to a first-order linear reconstruction, it is perhaps not surprising that the coefficient accuracy and spatial resolution obtained is less than can be achieved using more computationally intensive recursive iterative methods.[10–13] Yet another element common to first-order reconstructions, especially for backreflection studies (e.g., brain imaging), is that the locations of recovered features are biased toward the tissue surface.[24] Currently available methods are thus either overly computationally intensive or produce solutions having less than ideal spatial and coefficient accuracies.

Taking cues from MRI, we have recently developed an image-correction procedure that is both computationally efficient (i.e., simple matrix multiplication) and provides for solutions that have substantially improved coefficient accuracy (usually by a factor of 10), object localization, and spatial resolution.[14–18] The correction kernel is a quantitative description of the convolution of spatial information inherent in linear operations. We have referred to this as an information spread function, which is analogous to a point-spread function. The details of this blurring and displacement are both target dependent and algorithm dependent. The converse consideration is worth noting. Demonstrating that spatial blurring and displacement occur with linear solvers raises the question of why we need to turn to nonlinear solvers to overcome a situation that can be addressed by using methods that inherently are more computationally efficient. As with any scheme, its practical utility is dependent on demonstrating sufficient robustness with targets of interest (e.g., 3D complex media), which is the focus of this paper.

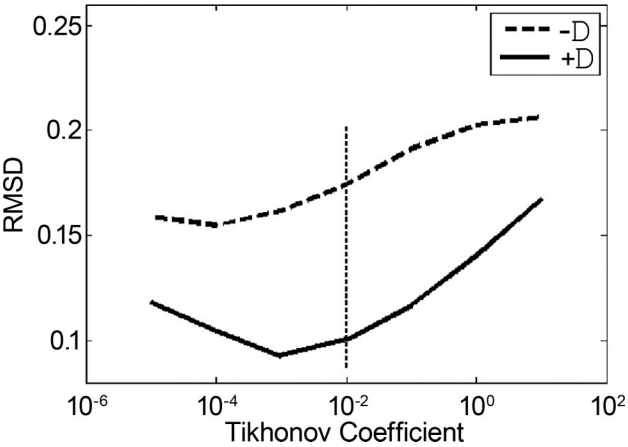


Fig. 9. Plot of rmsd versus Tikhonov regularization parameter λ, for the Target3–Reference3 combination and level-1 noise. The dotted vertical line indicates optimal value of λ, as derived from an L-curve analysis. −D = uncorrected image, +D = corrected image.

It has been suggested, in response to various presentations of these findings,[35–37] that the image correction achieved might well be attributable to the fact that a suboptimal degree of regularization was initially selected. As demonstrated in Fig. 9, we have directly tested this by using Tikhonov regularization parameters that straddle the optimal value as determined by an L-curve analysis. Inspection shows that in all cases, the corrected images are more accurate (i.e., lower spatial root-mean-squared difference between image and target media) than the uncorrected images.

The end point of functional imaging studies is not just the recovery of an image time series but the extraction of a variety of features. These features can serve as markers for disease,[38] as surrogates of other signals of interest that are not easily observable [e.g., BOLD (i.e., blood oxygen-level dependent) signal for neuroactivation],[39] or, in the case of state-space problems,[40] as the outputs of yet other more basic phenomenologies. Important to these interpretations is the question of how the known limitations of DOT impact on the extracted features. As mentioned, DOT images typically have low spatial resolution and, when limited to first-order solutions, can be spatially biased. A brute-force approach to addressing this concern might be to implement a recursive solver and apply it to the complete time series. Given current computing speeds, absent of a grid computing approach,[41] this would seem infeasible. Alternatively,

in an effort to retain computationally tractable solutions, one can ignore the additional spatial blurring and bias that first-order solutions introduce.

The aforementioned distortions can have significant effects on the information content derived from functional neuroimaging studies, which include identification of structure-function relationships in regions of interest and functional connectivities among end target tissues. In the case of the former, spatial bias can have the effect of displacing the response to areas outside of expected targeted areas. In contrast, blurring expands the area of activation but does not displace its centroid. These distortions can lead to mistaken association of areas that are not, in reality, functionally connected. It can also be expected that spatial bias and blurring will make it more difficult to correctly identify responses that are independent or uncorrelated, which are strategies commonly employed in functional neuroimaging studies.[42,43] Thus, when spatial distortions are ignored, conclusions based on subsequent analysis may be more difficult to justify.

In summary, we have demonstrated that the image-correction procedure described here is capable of computationally efficient reduction in the systematic spatial bias and blurring of first-order DOT images of complex 3D media. In the accompanying paper, we extend these findings to the correction of images of scattering coefficients and demonstrate improvements similar to those seen for absorption.[44]

This work was supported by the National Institutes of Health (NIH) under grants R21-HL67387, R21-DK63692, R41-CA96102, R41-NS050007, and R43-NS49734, and by the U.S. Army under grant DAMD017-03-C-0018.

## References

1. A. G. Yodh and B. Chance, "Spectroscopy and imaging with diffusing light," Phys. Today **48,** 34–40 (1995).
2. A. G. Yodh and D. A. Boas, "Functional imaging with diffusing light," in *Biomedical Photonics Handbook,* T. Vo-Dinh, ed. (CRC, 2003), pp. 21-1–21-45.
3. Y. Pei, H. L. Graber, and R. L. Barbour, "Influence of systematic errors in reference states on image quality and on stability of derived information for dc optical imaging," Appl. Opt. **40,** 5755–5769 (2001).
4. Y. Pei, H. L. Graber, and R. L. Barbour, "Normalized-constraint algorithm for minimizing inter-parameter crosstalk in DC optical tomography," Opt. Express **9,** 97–109 (2001).
5. H. L. Graber, Y. Pei, and R. L. Barbour, "Imaging of spatio-temporal coincident states by DC optical tomography," IEEE Trans. Med. Imaging **21,** 852–866 (2002).
6. G. S. Landis, T. F. Panetta, S. B. Blattman, H. L. Graber, Y. Pei, C. H. Schmitz, and R. L. Barbour, "Clinical applications of dynamic optical tomography in vascular disease," in *Optical Tomography and Spectroscopy of Tissue IV,* B. Chance, R. R. Alfano, B. J. Tromberg, M. Tamura, and E. M. Sevick-Muraca, eds., Proc. SPIE **4250,** 130–141 (2001).
7. R. L. Barbour, H. L. Graber, Y. Pei, and C. H. Schmitz, "Imaging of vascular chaos," in *Optical Tomography and Spectroscopy of Tissue IV,* B. Chance, R. R. Alfano, B. J. Tromberg, M. Tamura, and E. M. Sevick-Muraca, eds., Proc. SPIE **4250,** 577–590 (2001).
8. C. H. Schmitz, D. P. Klemer, R. E. Hardin, M. S. Katz, Y. Pei, H. L. Graber, M. B. Levin, R. D. Levina, N. A. Franco, W. B. Solomon, and R. L. Barbour, "Design and implementation of dynamic near-infrared optical tomographic imaging instrumentation for simultaneous dual-breast measurements," Appl. Opt. **44,** 2140–2153 (2005).
9. C. H. Schmitz, H. L. Graber, Y. Pei, M. B. Farber, M. Stewart, R. D. Levina, M. B. Levin, Y. Xu, and R. L. Barbour, "Dynamic studies of small animals with a four-color DOT imager," Rev. Sci. Instrum. **76,** 094302 (2005).
10. K. D. Paulsen and H. Jiang, "Spatially varying optical property reconstruction using a finite element diffusion equation approximation," Med. Phys. **22,** 691–701 (1995).
11. S. R. Arridge and J. C. Hebden, "Optical imaging in medicine II: modelling and reconstruction," Phys. Med. Biol. **42,** 841–853 (1997).
12. A. H. Hielscher, A. D. Klose, and K. M. Hanson, "Gradient-based iterative image reconstruction scheme for time-resolved optical tomography," IEEE Trans. Med. Imaging **18,** 262–271 (1999).
13. J. P. Culver, R. Choe, M. J. Holboke, L. Zubkov, T. Durduran, A. Slemp, V. Ntziachristos, B. Chance, and A. G. Yodh, "Three-dimensional diffuse optical tomography in the parallel plane transmission geometry: evaluation of a hybrid frequency domain/continuous wave clinical system for breast imaging," Med. Phys. **30,** 235–247 (2003).
14. H. L. Graber, R. L. Barbour, and Y. Pei, "Quantification and enhancement of image reconstruction accuracy by frequency encoding of spatial information," in *OSA Biomedical Topical Meetings, OSA Technical Digest* (Optical Society of America, 2002), pp. 635–637.
15. R. L. Barbour, H. L. Graber, Y. Xu, Y. Pei, and R. Aronson, "Strategies for imaging diffusing media," Transp. Theory Stat. Phys. **33,** 361–371 (2004).
16. H. L. Graber, Y. Xu, Y. Pei, and R. L. Barbour, "Spatial deconvolution technique to improve the accuracy of reconstructed three-dimensional diffuse optical tomographic images," Appl. Opt. **44,** 941–953 (2005).
17. Y. Xu, H. L. Graber, Y. Pei, and R. L. Barbour, "Improved accuracy of reconstructed diffuse optical tomographic images by means of spatial deconvolution: two-dimensional quantitative characterization," Appl. Opt. **44,** 2115–2139 (2005).
18. Y. Xu, Y. Pei, H. L. Graber, and R. L. Barbour, "Image quality improvement via spatial deconvolution in optical tomography: time-series imaging," J. Biomed. Opt. **10,** 051701 (2005).
19. http://www.mathworks.com/matlabcentral/fileexchange/loadFile.do?objectId=4879.
20. F. X. Castellanos, A. Di Martino, H. L. Graber, Y. Pei, C. H. Schmitz, and R. L. Barbour, "Dynamic optical tomography of cerebral vascular hemodynamics," Poster no. 650 at *Human Brain Mapping 2003* (New York, N.Y., 18–22 June 2003).
21. http://gid.cimne.upc.es/intro/.
22. A. Y. Bluestone, G. Abdoulaev, C. H. Schmitz, R. L. Barbour, and A. H. Hielscher, "Three-dimensional optical tomography of hemodynamics in the human head," Opt. Express **9,** 272–286 (2001).
23. F. A. Duck, *Physical Properties of Tissue: A Comprehensive Reference Book* (Academic, 1990).
24. D. A. Boas, A. M. Dale, and M. A. Franceschini, "Diffuse optical imaging of brain activation: approaches to optimizing image sensitivity, resolution, and accuracy," Neuroimage **23,** s275–s288 (2004).
25. H. L. Graber, J. Chang, R. Aronson, and R. L. Barbour, "A perturbation model for imaging in dense scattering media: derivation and evaluation of imaging operators," in *SPIE Institute of Medical Optical Tomography: Functional Imaging and Monitoring* (SPIE, 1993), Vol. IS11, pp. 121–143.
26. H. L. Graber, J. Chang, and R. L. Barbour, "Imaging of multiple targets in dense scattering media," in *Experimental and*

*Numerical Methods for Solving Ill-Posed Inverse Problems: Medical and Nonmedical Applications,* Proc. SPIE **2570,** 219–234 (1995).
27. X. Gu, Y. Xu, and H. Jiang, "Mesh-based enhancement schemes in diffuse optical tomography," Med. Phys. **30,** 861–869 (2003).
28. H. Jiang, "Frequency-domain fluorescent diffusion tomography: a finite-element-based algorithm and simulations," Appl. Opt. **37,** 5337–5343 (1998).
29. R. L. Barbour, H. L. Graber, R. Aronson, and J. Lubowsky, "Model for 3-D optical imaging of tissue," in *International Geoscience and Remote Sensing Symposium (IGARSS)* (1990), Vol. 2, pp. 1395–1399.
30. R. Aronson, R. L. Barbour, J. Lubowsky, and H. L. Graber, "Application of transport theory to infra-red medical imaging," in *Operator Theory: Advances and Applications, Proceedings of the 11th International Conference on Transport Theory, Blacksburg Va., 22–26 May 1989* (Birkhauser-Verlag, 1991), Vol. 51, pp. 64–75.
31. S. R. Arridge, P. van der Zee, M. Cope, and D. T. Delpy, "Reconstruction methods for infrared absorption imaging," in *Time-Resolved Spectroscopy and Imaging of Tissues,* B. Chance, ed., Proc. SPIE **1431,** 204–215 (1991).
32. M. A. O'Leary, D. A. Boas, B. Chance, and A. G. Yodh, "Experimental images of heterogeneous turbid media by frequency-domain diffusing-photon tomography," Opt. Lett. **20,** 426–428 (1995).
33. M. Huang, T. Xie, N. G. Chen, and Q. Zhu, "Simultaneous reconstruction of absorption and scattering maps with ultrasound localization: feasibility study using transmission geometry," Appl. Opt. **42,** 4102–4114 (2003).
34. N. L. Everdell, A. P. Gibson, I. D. C. Tullis, T. Vaithianathan, J. C. Hebden, and D. T. Delpy, "A frequency multiplexed near infrared topography system for imaging functional activation in the brain," Rev. Sci. Instrum. **76,** 093705 (2005).
35. Y. Xu, Y. Pei, H. L. Graber, and R. L. Barbour, "Improved accuracy of reconstructed diffuse optical tomographic images via spatial deconvolution: recent developments," Poster no. 83 at *Fourth Inter-Institute Workshop on Optical Diagnostic Imaging from Bench to Bedside at the National Institutes of Health* (Bethesda, Md., 20–22 September 2004).
36. Y. Xu, H. L. Graber, Y. Pei, and R. L. Barbour, "Spatial deconvolution of 3-D diffuse optical tomographic time series: influence of background medium heterogeneity," Poster no. 686 T-PM at *Human Brain Mapping 2006* (Florence, Italy, 11–15 June 2006).
37. H. L. Graber, Y. Xu, Y. Pei, and R. L. Barbour, "Image enhancement by linear spatial deconvolution: recent developments," Poster no. 77 at *Fifth Inter-Institute Workshop on Optical Diagnostic Imaging from Bench to Bedside at the National Institutes of Health* (Bethesda, Md., 25–27 September 2006).
38. U. Wolf, M. Wolf, J. H. Choi, M. Levi, D. Choudhury, S. Hull, D. Coussirat, L. A. Paunescu, L. P. Safonova, A. Michalos, W. W. Mantulin, and E. Gratton, "Localized irregularities in hemoglobin flow and oxygenation in calf muscle in patients with peripheral vascular disease detected with near-infrared spectrophotometry," J. Vasc. Surg. **37,** 1017–1026 (2003).
39. N. K. Logothetis, "The underpinnings of the BOLD functional magnetic resonance imaging signal," J. Neurosci. **23,** 3963–3971 (2003).
40. B. Alacam, B. Yazici, X. Intes, and B. Chance, "Extended Kalman filtering for the modeling and analysis of ICG pharmacokinetics in cancerous tumors using NIR optical methods," IEEE Trans. Biomed. Eng. **53,** 1861–1871 (2006).
41. C. J. Long, P. L. Purdon, S. Temereanca, N. U. Desai, M. Hamalainen, and E. N. Brown, "Large scale Kalman filtering solutions to the electrophysiological source localization problem: a MEG case study," at the *28th IEEE EMBS Annual International Conference* (IEEE, 2006), paper SaB02.5.
42. A. Hyvärinen, J. Karhunen, and E. Oja, *Independent Component Analysis* (Wiley, 2001).
43. M. Stetter, *Exploration of Cortical Function* (Kluwer Academic, 2002).
44. H. L. Graber, Y. Xu, and R. L. Barbour, "Image correction scheme applied to functional diffuse optical tomography scattering images," Appl. Opt. **46,** 1705–1716 (2007).